

## Flow reversal inside a drop evaporating on a soluble substrate

Alexandra Mailleur <sup>1</sup>, Jean Colombani <sup>1,\*</sup>, Christophe Pirat,<sup>1</sup>  
Charlotte Rivière,<sup>1</sup> and Irina Vodolazskaya <sup>2</sup>

<sup>1</sup>*Institut Lumière Matière; Université de Lyon; Université Claude Bernard Lyon 1; CNRS UMR 5306; Campus de la Doua, F-69622 Villeurbanne, France*

<sup>2</sup>*Laboratory of Mathematical Modeling, Astrakhan State University, Astrakhan, 414056, Russia*



(Received 4 April 2022; accepted 1 September 2022; published 19 September 2022)

The evaporation of drops of pure water on soluble substrates of salt leads to the growth of unprecedented hollow peripheral deposits. We report here on the experimental determination and numerical simulation of the flows inside a drop in this configuration. The velocity field is measured experimentally by a microparticle image velocimetry technique and is simulated using the hydrodynamics equations solved by the finite-elements method. The flow is characterized by an inward motion at the beginning of the evaporation, that is progressively replaced by an outward motion until the end of the evaporation. The transition between the two flow regions takes the form of a stagnation line, where the radial component of the velocity vanishes. This line migrates from the periphery toward the center of the drop, inducing the progressive inversion of the flow. The comparison between the experiments and simulations leads to the following interpretation of this flow reversal. The dissolution of the substrate induces the creation of a surface tension gradient at the drop free-surface, leading to an outward Marangoni flow along the drop surface and an inward flow near the substrate. As the diffusion progressively makes the concentration more uniform, this surface-driven convection stops and is replaced by the standard coffee-stain outward capillary flow.

DOI: [10.1103/PhysRevFluids.7.093605](https://doi.org/10.1103/PhysRevFluids.7.093605)

### I. INTRODUCTION

The exponential growth of the number of works devoted to the evaporation of sessile drops during the past two decades may be attributed to the omnipresence of the phenomenon [1]. Drops indeed evaporate on substrates in nature, in everyday life, as much as in industrial processes [2]. If the evaporating liquid is not pure, and contains solutes, colloids, or polymers, then a deposit is left on the surface, generally in the form of a coffee stain [3]. This phenomenon may be both detrimental, in the case of heritage degradation by rain [4] or stain formation in ultraclean processes [5], but can also be of great help for DNA mapping [6], innovative medical tests [7], nanolithography [8], or ink-jet printing [9].

This intense activity has brought a better knowledge of the interplay between the numerous mechanisms interacting during this apparently simple phenomenon. For instance, the flow patterns in the atmosphere around a droplet evaporating on a heated surface and its influence on the evaporation rate is now well understood [10]. The existence of Rayleigh [11], or Marangoni [12], or both flows [13] inside evaporating two-component drops, driven by concentration gradients, is also well established.

---

\*[jean.colombani@univ-lyon1.fr](mailto:jean.colombani@univ-lyon1.fr)

A configuration has held particular attention, in which the substrate is made of a thin film of polymer spin-coated on a flat surface [14], or more rarely is made of a bulk polymer [15], and the drop contains a solvent of the polymer. Here in addition to the above-mentioned mechanisms, the evaporated solvent may also be adsorbed by the substrate surrounding the drop, the substrate may swell by solvent uptake, it may dissolve in the drop, the solution may gel and the triple line may be subject to pinning-depinning. These studies are sometimes inspired by applications, because the pattern left by such drops on polymer layers may be used for device manufacturing in optoelectronics [16], or because this situation may be encountered with hydrosoluble polymers in the food industry [17,18].

To investigate the influence of the sole dissolution of a soluble substrate in an evaporating drop, compared to an inert substrate, without adsorption, solvent uptake, or gelation, we have recently studied the evaporation of a water drop on a mineral substrate, namely a salt crystal. In this configuration, the transport of the components of the dissolved salt toward the edge of the drop, and their precipitation at the liquid-air interface, leads to the formation of unexpectedly hollow rims [19].

To better understand the formation of these peculiar patterns, we investigate here both experimentally and numerically the inner flows during the evaporation of a drop of pure water on a salt substrate. Using microparticle image velocimetry in a confocal microscope, we measure the velocity field evolution inside a water drop evaporating on a heated dissolving salt substrate and compare it with numerical simulations of the phenomenon. The main conclusion of this study is that, in the course of the evaporation, a flow inversion occurs inside the drop. This reversal is revealed by the presence of a circular stagnation line propagating from the edge toward the center of the drop. Thanks to the experiment-simulation confrontation, we interpret this reversal as a consequence of the change of leading mechanism: Marangoni convection occurs at the very beginning of the phenomenon, whereas a capillary outward flow dominates afterwards, leading eventually to the formation of the ring deposit.

## II. EXPERIMENTS

### A. Experimental setup

The substrates are  $10 \times 10 \times 1 \text{ mm}^3$  samples of NaCl single crystals, polished with grit size down to  $1 \text{ }\mu\text{m}$ , to guarantee a good reproducibility of the surface roughness, hence of the drop contact angle. The samples are cleared from dust with compressed air and stored in a dessicator before use. The evaporating liquid is ultrapure water. The substrate is embedded in a heating device which allows to investigate substrate temperatures in the  $20$  to  $70^\circ\text{C}$  range. The relative humidity (RH) is monitored during the experiments. Microparticle image velocimetry ( $\mu$ -PIV) measurements in the evaporating drops are performed with a Leica SP5 inverted confocal microscope. In the course of the experiment, a drop of volume  $\sim 1 \text{ }\mu\text{l}$  seeded with  $1 \text{ }\mu\text{m}$  fluorescent beads (FluoSpheres carboxylate-modified microspheres yellow-green with an excitation wavelength of  $505 \text{ nm}$  and an emission wavelength of  $515 \text{ nm}$ ) is deposited on a flat and horizontal salt substrate. Images are obtained with a  $10\times$  N.A. 0.3 air objective, which gives approximately an observation window of  $1 \times 1 \text{ mm}^2$  in a plane parallel to the solid surface. The size of the pinhole is fixed to 1 Airy unit that provides a depth of field of  $11 \text{ }\mu\text{m}$ . Afterwards the in-plane colloid velocity field is obtained during the evaporation by following the average correlation method [20] with a home made Matlab code, to reduce errors due to Brownian motion and to achieve a higher signal-to-noise ratio.

### B. Evaporation scenario and associated kinetics

Once the drop is deposited, the evaporation proceeds in four steps. First, due to the very high dissolution rate of the salt, the substrate is immediately etched by the water, which induces an instantaneous anchoring of the triple line [Fig. 1 (left)]. The evaporation therefore remains in the constant-radius regime, with no initial receding phase, unlike the case of nanodroplets of water on

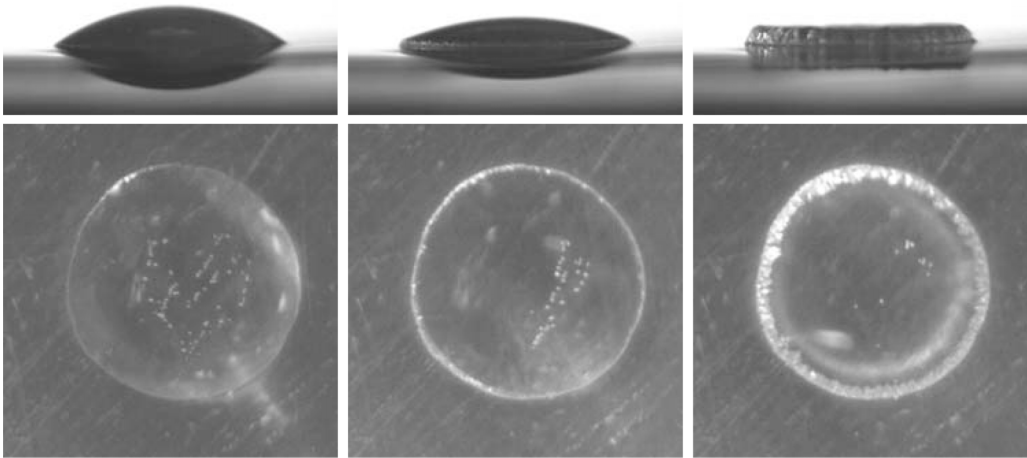


FIG. 1. Side and top view of a water drop, of sessile diameter  $d = 1.85$  mm, evaporating on a NaCl single crystal at  $T = 55^\circ\text{C}$  and  $\text{RH} = 45\%$  for elapsed times  $t = 2, 13,$  and  $34$  s from left to right.

silicon wafer, where the reaction between water and silicon is too slow to induce an immediate pinning of the triple line [5]. Second, a peripheral deposit is observed to form at the edge of the drop. Thus, the contact line leaves the initial perimeter of the drop and moves inward, following the growing ring deposit [Fig. 1 (middle)], and the apex continues to lower [Fig. 1 (right)]. In the third step, the evaporation is such that the apex of the drop reaches the substrate and starts to recede outwards by dewetting (Fig. 2). Finally, the inner triple line reaches the peripheral deposit, which in the majority of cases can roll-up and close, forming a hollow shell, inside which the remaining liquid continues to evaporate.

Before investigating the inner flow, the evaporation kinetics is estimated from the evolution of the drop volume. Figure 3 exhibits the change with time of the normalized drop volume during the pinned triple line regime, i.e., before the rim starts to depart visibly from the substrate and grow. It can be seen that for four sample temperatures, the volume decreases linearly with time, as expected. Indeed, the evaporation rate  $dV/dt$  is known to be proportional to the drop sessile radius  $r_w$ , not

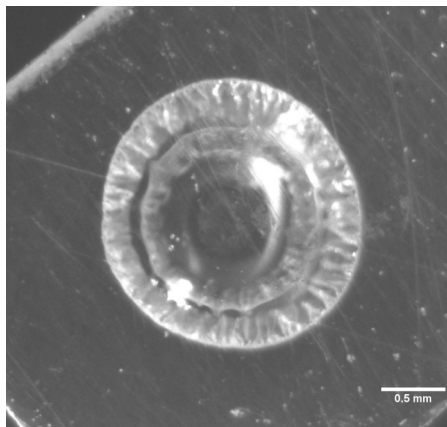


FIG. 2. Central dewetting at the end of the evaporation in the experiment of Fig. 1. The substrate is now visible at the center of the drop.

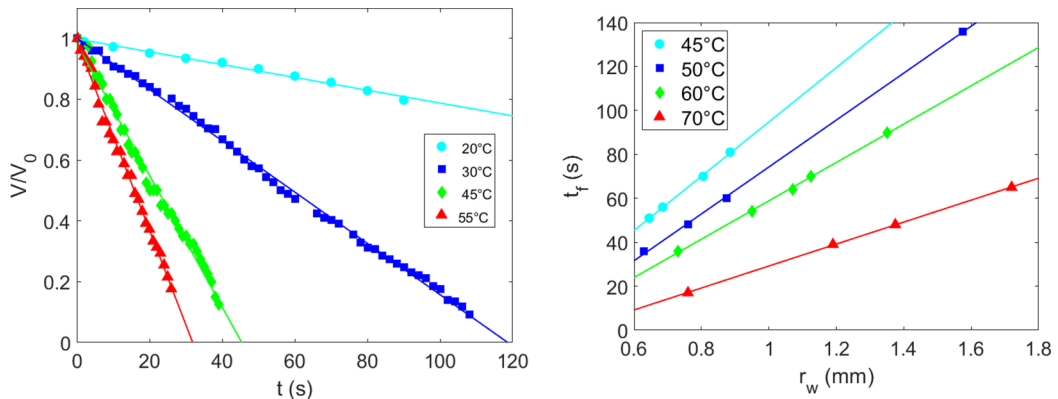


FIG. 3. Left: Time evolution of the volume  $V$ , normalized by the initial volume  $V_0$ , of water drops (initial sessile radius  $r_w \approx 0.6$  mm, initial contact angle  $\theta_0 \approx 45^\circ$ ) evaporating on NaCl single crystals at temperature 20 (cyan circles), 30 (blue squares), 45 (green diamonds), and 55°C (red triangles) for  $\text{RH} \approx 30\%$ . Right: Evaporation time  $t_f$  as a function of the drop sessile radius  $r_w$  at temperature 45 (cyan circles), 50 (blue squares), 60 (green diamonds), and 70°C (red triangles). The initial contact angle for all drops is  $\theta_0 \approx 45^\circ$ . The straight lines are guides for the eyes.

to its evaporating surface area, as a consequence of the diffusion-limited nature of the evaporation [21]. As the triple line is initially pinned,  $r_w$  remains constant, so does  $dV/dt$ , and the evaporation regime is linear.

The total evaporation time  $t_f$  is a characteristic parameter of the phenomenon which is required to make the simulations cope with the experiments (see Sec. III A). As the evaporation scenario is complex, the determination of  $t_f$  is not straightforward. Here we choose to estimate each  $t_f$  as the time at which the extrapolation of the  $V(t)/V_0$  curve reaches the value  $V/V_0 = 0$  [Fig. 3 (left)]. Figure 3 (right) shows the change of the total evaporation time with the sessile drop radius for some investigated temperatures. This evaporation time is seen to increase linearly with the drop radius and the slope of the  $t_f(r_w)$  lines is diminishing when the temperature increases.

### C. Internal flows

The velocity field is measured by  $\mu$ -PIV in a plane parallel and close to the solid-liquid interface for several temperatures (see video in the Supplemental Material [22]). In all measurements, the fluid initially experiences an uniform inward motion. Within a few tens of seconds, a stagnation line forms at the edge of the drop, where the fluid is seen to be at rest. This line moves progressively inward, splitting the velocity field into two parts. Inside the line, the fluid continues to move inward. Outside, the liquid exhibits a different behavior, showing an outward motion (see Fig. 4). Once the stagnation line has reached the center of the drop, it disappears and the in-plane flow is seen purely outward.

The mean radial velocity  $\langle v_r \rangle$ , averaged along circles of radius  $r$ , exhibits at the beginning of the experiment negative values, corresponding to an inward motion as shown in Fig. 5. Then positive values appear close to the drop periphery, i.e., at  $r = r_w$ , corresponding to the initiation of an outward flow. Between the negative and positive values, the crossing of the  $\langle v_r \rangle = 0$  line by the curve corresponds to the position of the stagnation line  $r_{st}$ . With time, this crossing of the abscissa axis is seen to move leftward, showing the movement of the stagnation line toward the drop center. The latest times exhibit purely positive values, when the fluid motion is exclusively centrifugal.

Figure 6 shows the evolution of the stagnation line position for various temperatures. After a transient period of a few seconds corresponding to the drop installation, the line is observed to accelerate slightly during its displacement.

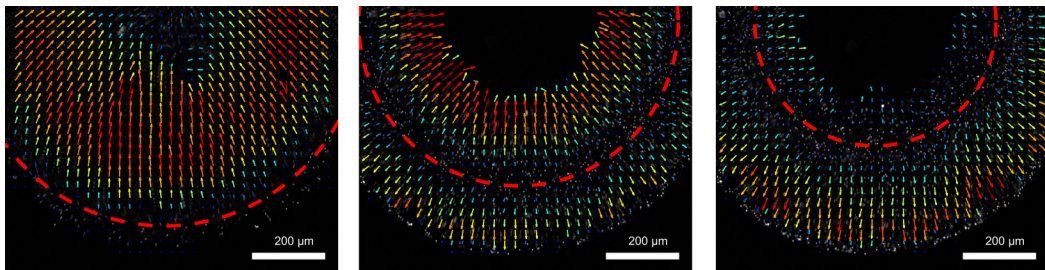


FIG. 4. In-plane velocity field ( $5 \pm 5$ )  $\mu\text{m}$  above the bottom of a drop of pure water of sessile diameter 1.2 mm seeded with fluorescent beads evaporating on a NaCl single crystal, from left to right, 10, 27, and 33 s after deposition. The color indicates the increasing magnitude, from blue to red, together with the length of the arrows. The red dashed line shows the stagnation line.

### III. SIMULATIONS

#### A. Analytical model

The drops have always been observed to keep a circular shape. Therefore the simulated drop has been considered to show an axis of rotation and the problem has been solved in the two-dimensional coordinate system  $(r, z)$  (Fig. 7). The radius of the droplet base is always of the order  $r_w \sim 10^{-3}$  m. As the drops have always been observed to be immediately pinned once deposited, this radius has been kept constant throughout the modeling time. The height of the drop apex at the beginning of evaporation is of the order  $h(0, 0) \sim 10^{-4}$  m.

For a water drop of the specified size, the capillary number  $\text{Ca} = \mu v / \sigma$ , for the characteristic flow velocity  $v \ll 10^2$  m/s shown in Fig. 5 (here  $\mu \sim 10^{-3}$  Pa s is the dynamic viscosity and  $\sigma \sim 10^{-1}$  N/m the surface tension of the liquid) and the Bond number  $\text{Bo} = \Delta \rho g h^2 / \sigma$  (here  $g \sim 10$  m/s<sup>2</sup> is the acceleration of gravity and  $\Delta \rho \sim 10^3$  kg/m<sup>3</sup> is the difference in density of water and

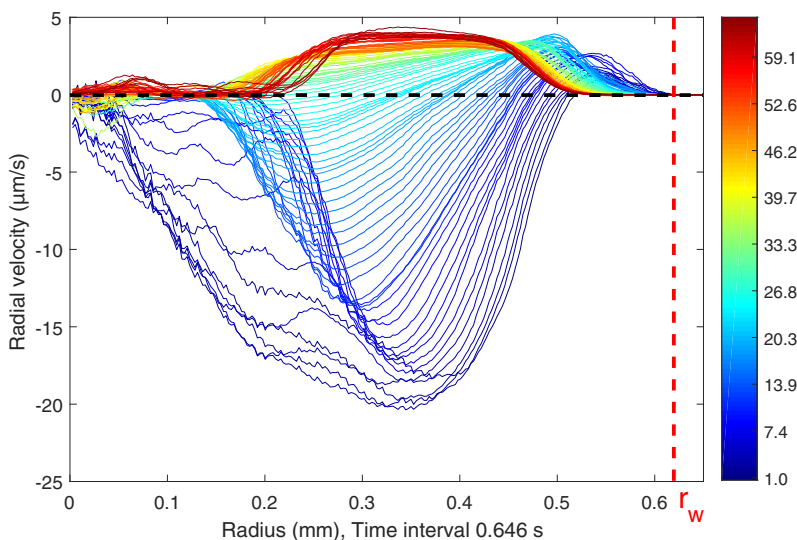


FIG. 5. Mean radial velocity  $\langle v_r \rangle$  of the flow inside the drop along the radius  $r$  in the drop deduced from the  $\mu$ -PIV measurements of Fig. 4. The colors give the elapsed time since deposition for each curve and refer to the color-bar with the time given in seconds. Positive (negative) values stand for outward (inward) radial velocity components.

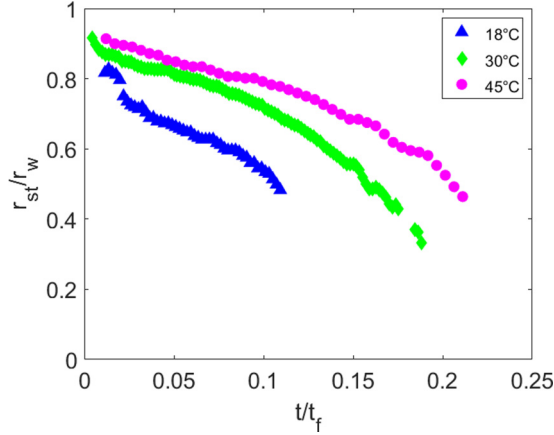


FIG. 6. Dependence of the stagnation line position on time at 18 (blue triangles), 30 (green diamonds), and 45°C (pink circles). After a transient period of a few seconds, the line is observed to accelerate slightly during its displacement. The position is normalized by the drop sessile radius and the time by the total evaporation time.

air) are always much smaller than one. Therefore the capillary forces always exceed all other forces. So we have considered the liquid-air interface  $h(r, t)$ , the free surface of the drop, as a spherical segment and we have used the parabolic approximation for simplicity  $h(r, t) = h(0, t)[1 - (r/r_w)^2]$ .

The substrate temperature is kept constant and equal to or higher than the ambient temperature. Nonetheless, two heat sources are present inside the drop for the entire duration of the phenomenon, due to the double phase change. Both the dissolution of the salt and the evaporation of water are endothermal mechanisms, which may induce a temperature decrease of the drop. However, the characteristic time of the heat transfer in a drop of this size is  $\tau_T = h(0, 0)^2/\lambda \sim 0.1$  s ( $\lambda \sim 10^{-7}$  m<sup>2</sup>/s is the thermal diffusivity of water). The characteristic salt diffusion time is  $\tau_D = h(0, 0)^2/D \sim 10$  s ( $D \sim 10^{-9}$  m<sup>2</sup>/s is the diffusion coefficient of NaCl components in water). The drying time of the drop  $t_f$  depends on the substrate temperature and on the drop size and ranges from  $\sim 10$  to  $\sim 100$  s (see Fig. 3 right). Therefore the temperature equalization time  $\tau_T$  is at least two orders of magnitude shorter than the drying time  $t_f$  and the salt diffusion time  $\tau_D$ . Furthermore, the thermal conductivity of the salt substrate is known to be one order of magnitude higher than the thermal conductivity of the aqueous salt solution, thereby accelerating even more the thermal equilibration of the drop. Consequently, both the solid and liquid contribute to homogenize the temperature inside the drop quasi instantaneously, thus making the presence of thermal gradients unlikely. For this reason, the

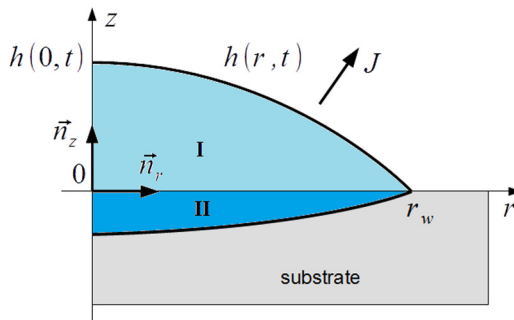


FIG. 7. Model of the drop evaporating on a soluble substrate: coordinate system.

temperature of the drop  $T$  is assumed to be uniform, and potential thermal effects, like thermal Marangoni convection, are not taken into account in the model.

To elaborate a simple but complete model of the drop evaporation, the determination of the respective part of diffusion and convection in the distribution of the salt concentration is first necessary. This balance can be evaluated from the Péclet number  $Pe = v_z h(0, 0)/D$ , with  $v_z$  the vertical component of the fluid velocity. This latter quantity can be estimated from the radial component of the velocity  $v_r$  via  $v_z \sim v_r h(0, 0)/r_w$ . As can be observed in Fig. 5, the experiments exhibit  $v_r$  values of the order of  $10 \mu\text{m/s}$ , therefore  $v_z \sim 1 \mu\text{m/s}$ , which induces  $Pe = 10^{-1}$ .

Therefore the convective transport of salt plays a secondary role compared to diffusion and the distribution of the salt concentration  $C = m_{\text{NaCl}}/(m_{\text{NaCl}} + m_{\text{water}})$  ( $m_{\text{NaCl}}$  and  $m_{\text{water}}$  are the mass of salt and water in the solution) in the droplet was calculated using the diffusion equation in the special case when the change of density of the solution and the change of diffusion coefficient of salt dissolved in water are negligible:

$$\frac{\partial C}{\partial t} = D \operatorname{div}(\operatorname{grad} C). \quad (1)$$

The initial and boundary conditions for the salt concentration are  $C(t = 0) = 0$  and  $C(z = 0) = C_{\max}$ ,  $C_{\max}$  being the concentration of the saturated salt solution. Indeed, even though the exact dissolution rate of NaCl is not known, it is accepted that the chemical reaction is so fast compared to the mass transport of the released ions in the drop that the solution remains always saturated at the interface, whatever the shape of the latter [23]. Regarding the concentration gradient,  $dC/dn = JC/(\rho D)$  on the liquid-air interface (the condition for the absence of accumulation of salt particles at the moving boundary) and  $dC/dr = 0$  on the symmetry axis ( $\mathbf{n}$  is a vector normal to the drop surface,  $J$  is the evaporation rate and  $\rho$  the density of water).

The velocity field,  $\mathbf{v} = v_r \mathbf{n}_r + v_z \mathbf{n}_z$ , in the droplet was calculated at different times using the Navier-Stokes equation for incompressible liquid in the lubrication approximation [24]. The evaporation rate was taken as  $J(r) = \frac{J_0}{\sqrt{1-(r/r_w)^2}}$  [25].  $J_0$  can be determined using the evaporation time  $t_f$ , considering that the whole volume of water evaporates during the time  $t_f$ :

$$t_f \int_0^{r_w} 2\pi r J dr \approx \frac{\rho_{\text{water}} \pi h(0, 0) r_w^2}{2} \implies J_0 \approx \frac{\rho_{\text{water}} h(0, 0)}{2t_f}. \quad (2)$$

Here  $\rho_{\text{water}}$  is the density of water.

The absence of flows was assumed in the region of dissolution of the substrate (region II in Fig. 7). The conditions for velocity were as follows:  $v_r = 0$  and  $v_z = 0$  at  $z = 0$ ,  $\frac{\partial v_r}{\partial z} + \frac{\partial v_z}{\partial r} = \frac{1}{\mu} \frac{\partial \sigma}{\partial r}$ , and  $v_z = \frac{\partial h(r, t)}{\partial t} + \frac{J}{\rho}$  at  $z = h(r, t)$ . Also averaging over the droplet height the  $r$  component of the velocity, we get [25]

$$\langle v_r \rangle = \frac{1}{h} \int_0^h v_r dz = -\frac{1}{rh} \int_0^r r \left( \frac{J}{\rho} + \frac{\partial h}{\partial t} \right) dr, \quad (3)$$

and using the continuity equation  $\operatorname{div} \mathbf{v} = 0$ , we can derive expressions for  $v_r$  and  $v_z$ :

$$v_r = \left\{ \frac{1}{\mu} \frac{\partial \sigma}{\partial r} + \frac{2r}{r_w^2} \frac{\partial h(0, t)}{\partial t} - \frac{rJ_0}{\rho r_w^2 [1 - (r/r_w)^2]^{3/2}} \right\} \left[ \frac{3z}{h(r, t)} - 2 \right] \frac{z}{4} + \frac{3zr_w^2}{2rh^2(r, t)} \left[ \frac{z}{h(r, t)} - 2 \right] \left\{ \frac{J_0}{\rho} - \frac{J_0 \sqrt{1 - (r/r_w)^2}}{\rho} + \frac{r^2}{4r_w^2} \frac{\partial h(0, t)}{\partial t} [2 - (r/r_w)^2] \right\}, \quad (4)$$

$$\begin{aligned}
 v_z = & -\frac{z^2}{4} \left\{ \frac{1}{\mu r} \frac{\partial \sigma}{\partial r} + \frac{1}{\mu} \frac{\partial^2 \sigma}{\partial r^2} + \frac{4}{r_w^2} \frac{\partial h(0, t)}{\partial t} - \frac{J_0 [2 + (r/r_w)^2]}{\rho r_w^2 [1 - (r/r_w)^2]^{5/2}} \right\} \left[ \frac{z}{h(r, t)} - 1 \right] \\
 & - \frac{3z^2 h(0, t)}{h^3(r, t)} \left[ \frac{z}{h(r, t)} - 2 \right] \left\{ \frac{J_0}{\rho} - \frac{J_0 \sqrt{1 - (r/r_w)^2}}{\rho} + \frac{r^2}{4r_w^2} \frac{\partial h(0, t)}{\partial t} [2 - (r/r_w)^2] \right\} \\
 & - \left\{ \frac{1}{\mu} \frac{\partial \sigma}{\partial r} + \frac{2r}{r_w^2} \frac{\partial h(0, t)}{\partial t} - \frac{rJ_0}{\rho r_w^2 [1 - (r/r_w)^2]^{3/2}} \right\} \frac{z^3 r h(0, t)}{2h^2(r, t) r_w^2} \\
 & - \frac{z^2}{2h^2(r, t)} \left[ \frac{z}{h(r, t)} - 3 \right] \left\{ \frac{J}{\rho} + \frac{\partial h(0, t)}{\partial t} [1 - (r/r_w)^2] \right\}. \tag{5}
 \end{aligned}$$

The rate of decrease of the liquid-air interface at the apex  $h(0, t)$  can be estimated by assuming that it decreases due to the evaporation of water and to the dissolution of the salt substrate. The average rate of decrease in the height of the drop at the top due to evaporation is equal to  $\frac{h(0,0)}{t_f}$ . The change of the position of the liquid-air interface due to dissolution can be estimated from the mass conservation using the following assumptions: the volume occupied by the crystalline salt is filled with a saturated solution of this salt, the solution of the drop becomes saturated in a time approximately equal to the characteristic salt diffusion time  $\tau_D$ , and the liquid-substrate interface is a spherical segment. Thus, the depth of the pit in the center of the substrate is

$$h(0, 0) \frac{\rho_{\text{water}} C_{\text{max}}}{\rho_{\text{NaCl}} (1 - C_{\text{max}})} \approx 10^{-1} h(0, 0) \tag{6}$$

and

$$h(0, \tau_D) = h(0, 0) \frac{\rho_{\text{water}} (\rho_{\text{NaCl}} - \rho_{\text{sol}} C_{\text{max}})}{\rho_{\text{NaCl}} \rho_{\text{sol}} (1 - C_{\text{max}})}. \tag{7}$$

Here  $\rho_{\text{water}}$  is the density of water,  $\rho_{\text{NaCl}}$  is the density of NaCl crystal,  $\rho_{\text{sol}}$  is the density of a saturated aqueous solution of NaCl. The average rate of decrease in the drop apex due to dissolution is  $\frac{h(0,0) - h(0, \tau_D)}{\tau_D}$ . Hence one obtains  $h(0, t) = h(0, 0) - \left[ \frac{h(0,0)}{t_f} + \frac{h(0,0) - h(0, \tau_D)}{\tau_D} \right] t$  in linear approximation.

## B. Numerical computation details

Numerical calculations were carried out from the time when a clean drop of water was deposited onto the substrate, at  $t = 0$ , to the moment of time slightly exceeding  $\tau_D$ . The calculations were carried out by the finite element method using the program FlexPDE for region I (Fig. 7). The equations were reduced to a dimensionless form. The dimensionless quantities were determined as follows:  $\tilde{r} = r/r_w$ ,  $\tilde{z} = z/h(0, 0)$ ,  $\tilde{t} = t/t_f$ ,  $\tilde{h} = h/h(0, 0)$ ,  $\tilde{v}_r = v_r t_f / r_w$ ,  $\tilde{v}_z = v_z t_f / h(0, 0)$ , and  $\tilde{J}_0 / \rho = J_0 t_f / [\rho h(0, 0)]$ .

The physical properties of the solution, density  $\rho$ , viscosity  $\mu$ , and diffusion coefficient of the salt components in water  $D$ , are constant with concentration. The surface tension  $\sigma$  depends on the salt concentration  $C$  linearly [26]. The calculations were carried out for several temperatures within the range 20–60°C. At the first stage, the salt concentration in the solution was calculated [Eq. (1)]. At the second stage, the velocity field in the solution was determined [Eqs. (4) and (5)] taking into account the salt concentration gradient at the liquid-air interface. The values of the physical parameters of the pure water and of the aqueous solution of NaCl at different temperatures were taken from Refs. [26–30].

## C. Internal flows

Once the seeded drop of ultraclean water is placed onto the horizontal salt substrate, the latter dissolves. At the same time, the drop volume decreases due to evaporation. The reverse flow within



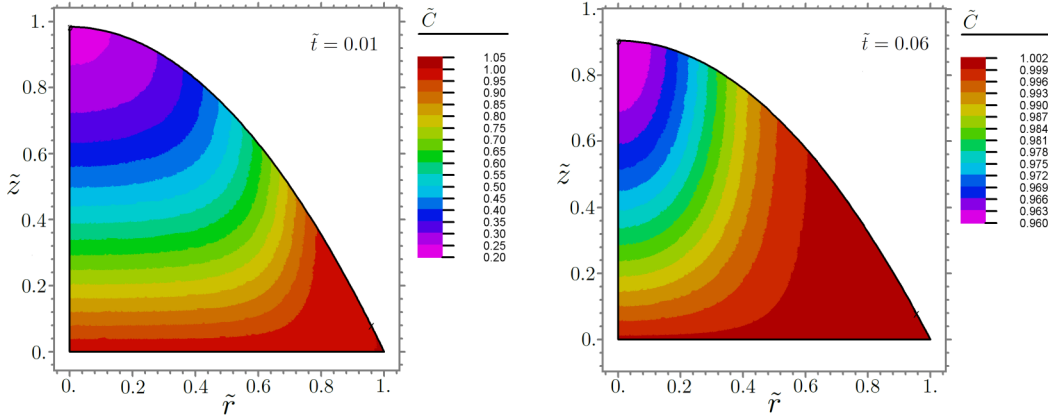


FIG. 8. Distribution of salt concentration  $C$  in the drop at  $T = 60^\circ\text{C}$  at  $t = 0.01t_f = 0.6$  s (left) and  $t = 0.06t_f = 3.6$  s (right), with  $t_f = 60$  s. The concentration is normalized by  $C_{\max}$ , and the coordinates  $r$  and  $z$  are normalized by  $r_w$  and  $h(0, 0)$ , respectively. The average concentration value, averaged over the drop, is  $\bar{C}_{\text{mean}} = 0.738478$  (left) and  $\bar{C}_{\text{mean}} = 0.994449$  (right).

the drop near the substrate, which is observed at the beginning of the experiments (Fig. 4), opposite to the regular outward capillary flow [3], may originate from the dependence of the surface tension on the salt concentration, i.e., from a solutal Marangoni flow. Indeed, the surface tension of the solution increases with an increase in the salt concentration. When the substrate starts to dissolve, immediately after placing the drop, the surface tension at the edge of the drop [for  $r \approx r_w$ , where  $h(r, t)$  is small] will be greater than at the center of the surface [for  $r \approx 0$ , where  $h(r, t)$  is larger]. Therefore, the Marangoni flow will be directed along the surface from the center toward the edge of the drop. Thus, near the substrate, the flow will be directed from the edge to the center to ensure the continuity of the flow [31].

Subsequently, the salt concentration in the solution will gradually equalize during the diffusion of the salt and the surface tension will become uniform after a time of the order of the characteristic

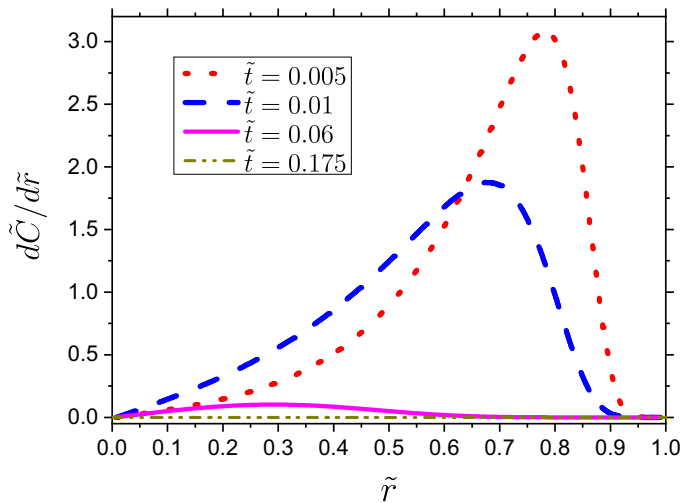


FIG. 9.  $r$  component of the salt concentration gradient on the liquid-air boundary of the drop of Fig. 8 at different times:  $0.005t_f = 0.3$  s,  $0.01t_f = 0.6$  s,  $0.06t_f = 3.6$  s,  $0.175t_f = 10.5$  s. The concentration is normalized by  $C_{\max}$  and the coordinate  $r$  by  $r_w$ .

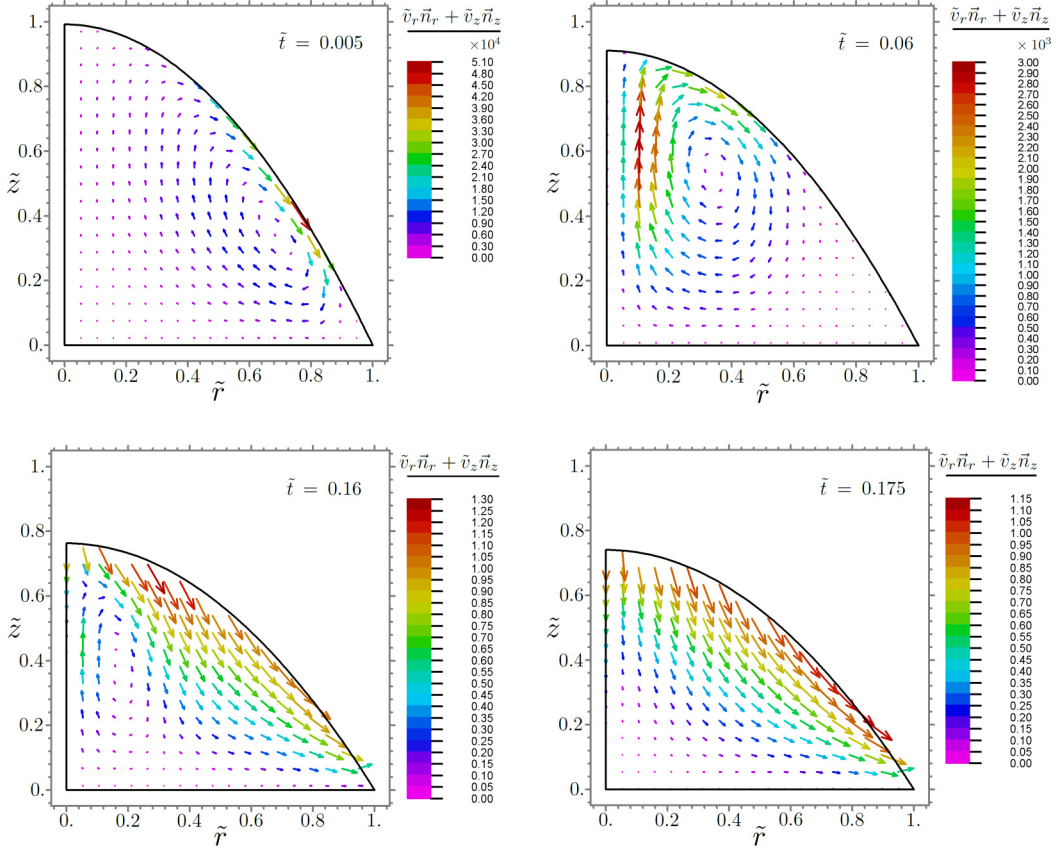


FIG. 10. Velocity field in the drop of Fig. 8 at times  $t = 0.005t_f = 0.3$  s,  $t = 0.06t_f = 3.6$  s,  $t = 0.16t_f = 9.6$  s, and  $t = 0.175t_f = 10.5$  s. The  $r$  component of the velocity  $v_r$  is normalized by  $r_w/t_f = 1.7 \times 10^{-5}$  m/s, the  $z$  component of the velocity  $v_z$  is normalized by  $h(0, 0)/t_f = 1.7 \times 10^{-6}$  m/s. There is a multiplicative factor of the velocity values of  $10^4$  at  $\tilde{t} = 0.005$  and  $10^3$  at  $\tilde{t} = 0.06$  in the color bar.

time of salt diffusion in water  $\tau_D$ , and the dominant flow at the solid-liquid interface will be directed towards the edge of the drop, as during evaporation on an inert substrate [3]. To validate or invalidate this interpretation, hydrodynamic simulations of the system, using the experimental parameters used as inputs, have been carried out.

In Figs. 8–11, the results of numerical calculations at  $T = 60^\circ\text{C}$  are shown. In the simulations, the radius of the drop base is  $r_w = 1.02 \times 10^{-3}$  m, the height of the drop apex at the beginning of evaporation is  $h(0, 0) = 0.1 \times 10^{-3}$  m, the drying time is  $t_f = 60$  s [cf. Fig. 3 (right)] and the characteristic salt diffusion time is  $\tau_D \approx 3$  s.

The salt concentration in the drop increases due to the dissolution of the substrate and becomes almost uniform during the first 10 s (see Fig. 8). The lines of constant concentration are curved and the distance between them is minimal at the liquid-air interface, where the concentration gradient exhibits therefore a maximum. This gradient decreases and shifts to the top of the drop with time, as shown in Fig. 9.

A vortex is observed in the velocity field, the center of which shifts with time to the center of the drop (Fig. 10). The moment of disappearance of the vortex was interpreted as the transition between the Marangoni regime, where the incoming flow is predominant, and the capillary regime, where the outgoing flow dominates. This moment occurs at time  $t_{tr} = 10.5$  s. To confirm this statement, we have additionally plotted the dependence of the velocity  $r$  component on the coordinate  $r$  at different

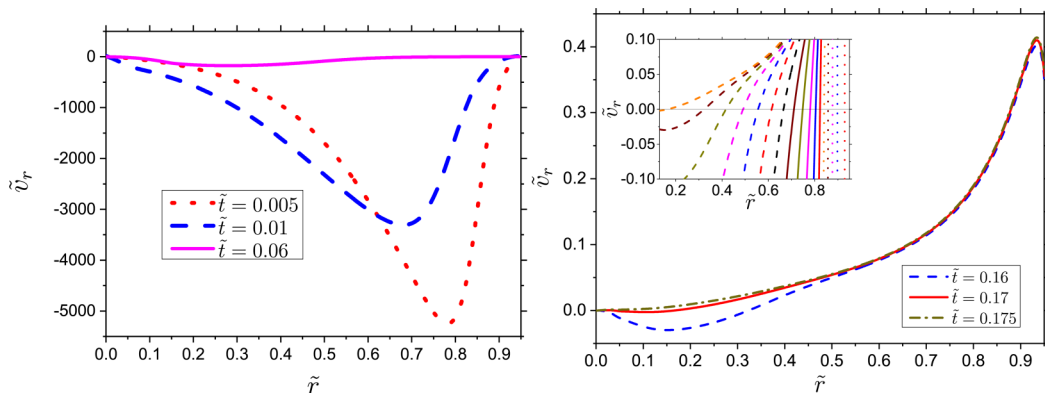


FIG. 11. Dependence of the  $r$  component of the velocity  $v_r$  on the  $r$  coordinate at the height  $h(0, t)/24$  in the drop of Fig. 8 at different times:  $0.005t_f = 0.3$  s,  $0.01t_f = 0.6$  s,  $0.06t_f = 3.6$  s (left),  $0.16t_f = 9.6$  s,  $0.17t_f = 10.2$  s, and  $0.175t_f = 10.5$  s (right). Inset: the same dependence for times from  $0.01t_f$  to  $0.17t_f$  (from right to left) with a step of  $0.01t_f$  in the neighborhood of  $v_r = 0$ , evidencing the inward motion of the stagnation line, i.e., of the intersection of the curves with the  $v_r = 0$  axis. The  $r$  component of the velocity  $v_r$  is normalized by  $r_w/t_f = 1.7 \times 10^{-5}$  m/s.

heights in the droplet at different times near the transition. At  $t_{tr}$ , when the flow regime changes, this velocity component takes on only nonnegative values, whatever the height (see Fig. S4 in the Supplemental Material [22]). The radial speed of the inward flow decreases with time [Fig. 11 (left)] before reversing progressively [insert of Fig. 11 (right)] and becoming uniformly and constantly outward [Fig. 11 (right)].

A similar analysis performed at  $20^\circ\text{C}$  can be found in Figs. S1–S5 of the Supplemental Material [22]. Figure S5 in particular exhibits values of the velocity without normalization. Whereas the lubrication model permits to keep all the necessary ingredients of the phenomenon in a tractable manner, thereby simulating the correct flow regimes, it is not intended to bring values in quantitative agreement with the experiments, as can be seen in comparing Figs. 5 and S5.

So far, the trends of the velocities from the numerical simulations are similar to the ones observed in the experiments and confirm our assumption of a change of leading hydrodynamic regime stemming from the concentration homogenization at the beginning of the evaporation.

#### IV. DISCUSSION

To get further in the experiment-simulation confrontation, Fig. 12 shows the dependence on time of the position of the point  $r_{st}$  at which the radial component of the velocity at height  $h(0, 0)/24$  vanishes ( $v_r = 0$ ) at  $20$  and  $45^\circ\text{C}$ , obtained from graphs similar to the inset in Fig. 11, and the experimental corresponding values from Fig. 6.

Regarding the crudeness of the assumptions, the similarity between the trend of the experimental and numerical  $r_{st}/r_w(t/t_f)$  curves is striking. Both exhibit the inward motion of the stagnation curve, with an inflection point sharing an initial slow movement and a faster migration at the end. Both results show that the temperature change does not modify the nature of the phenomenon but only its kinetics. This agreement supports the point that the ingredients included in the model (water evaporation, salt dissolution and diffusion, concentration dependence of the liquid surface tension) are sufficient to explain the flow patterns during the experiments.

To estimate the variability of the stagnation line motion with the drop size, numerical calculations were also performed at the two temperatures for a drop of radius  $r_w = 0.7$  mm (see Fig. S6 of the Supplemental Material [22]), which shows trends similar to the  $r_w = 1.02$  mm drop.

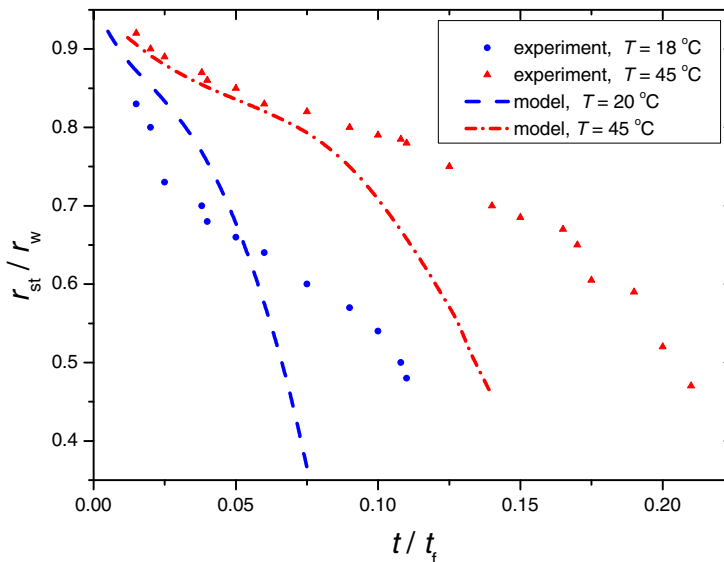


FIG. 12. The lines are the dependence of the radial position of the point  $r_{st}$  at which the radial component of the velocity [at height  $h(0, 0)/24$ ] vanishes ( $v_r = 0$ ), on time, at  $T = 20$  and  $45^\circ\text{C}$ . The coordinate  $r$  is normalized by  $r_w$  and the time  $t$  is normalized by  $t_f$ . The symbols correspond to the experimental data.

A schematic representation of the mechanisms explaining the flow reversal is shown in Fig. 13. It is worth mentioning that this process, based on a concentration effect, widens the possible source of flow inversion in evaporating drops. Indeed, two previous cases of stagnation line, close to the triple line, had been observed at the surface of a drop evaporating on an inert substrate. In the first case, for a pure water drop, this flow reversal had been interpreted as the consequence of the existence of a maximum temperature at a given height of the liquid-air interface [32]. This thermal peak induces a minimum of the surface tension gradient, which creates two opposite Marangoni streams, flowing away from this point, where the in-plane liquid velocity is vanishing. The second case also corresponds to a thermal Marangoni flow, stemming here from the previous heating of a colloidal suspension drop deposited on a nonheated substrate, competing with the usual capillary flow [33]. Therefore we have shown here that, not only thermal Marangoni flows, but also solutal Marangoni flows may induce a stream arrest during drop evaporation.

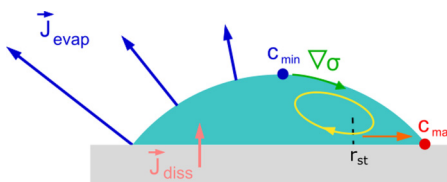


FIG. 13. Overall scheme of the flows inside the droplet. As the concentration  $C_{min}$  is smaller at the top of the droplet than the concentration  $C_{max}$  at the triple line, the concentration gradient induces a surface tension gradient (green arrow), so a Marangoni convection loop (yellow arrows), hindering the capillary outward coffee-stain flow (orange arrow). Starting from the three-phase line, the concentration gets progressively uniform, which stops the Marangoni flow. The vertical black dashed line at position  $r_{st}$  is the stagnation line between the Marangoni and coffee-stain flows.

## V. CONCLUSION

We have investigated the flows inside a drop evaporating onto a soluble substrate, both experimentally, with  $\mu$ -PIV measurements, and numerically, with finite-elements simulations of the hydrodynamic equations. A crossover has been observed between two regimes in the form of a flow reversal: at some point, an outward flow takes over the initial inward flow until the end of the evaporation. The crossover is characterized by a moving stagnation line, where the fluid radial velocity vanishes, starting from the edge and moving rapidly toward the center of the drop. Thanks to the confrontation of experiments and simulations, we have interpreted this behavior as a consequence of the change in the concentration field inside the drop. In the first regime, the salt starts to dissolve in the water drop. This dissolution generates a concentration gradient, which in turn induces a surface tension gradient at the drop-free surface, the tension being higher at the drop edge. This surface tension gradient leads to an outward Marangoni flow along the surface and an inward flow near the substrate. In a few tens of seconds, the concentration homogenizes, which stops the Marangoni flow. Subsequently, the expected centrifugal flow takes place, stemming from the pinning of the triple line, which requires a constant replenishing of the drop edge. This capillary flow contributes to the formation of the original hollow rims left by the evaporated drop in this peculiar configuration.

## ACKNOWLEDGMENTS

We thank O. Pierre-Louis for fruitful discussions, G. Simon, A. Piednoir, R. Fulcrand, and F. Gay for experimental help, and CNES (French Space Agency) and CNRS for financial support. The authors declare no conflict of interest.

- 
- [1] D. Brutin, ed., *Droplet Wetting and Evaporation* (Elsevier, Amsterdam, 2015)
  - [2] D. Zang, S. Tarafdar, Y. Y. Tarasevich, M. D. Choudhury, and T. Dutta, Evaporation of a droplet: From physics to applications, *Phys. Rep.* **804**, 1 (2019).
  - [3] R. Deegan, O. Bakajin, T. Dupont, G. Huber, S. Nagel, and T. Witten, Capillary flow as the cause of ring stains from dried liquid drops, *Nature (London)* **389**, 827 (1997).
  - [4] R. J. Flatt, F. Caruso, A. M. A. Sanchez, and G. W. Scherer, Chemomechanics of salt damage in stone, *Nat. Commun.* **5**, 4823 (2014).
  - [5] N. Belmiloud, A. H. Tamaddon, P. W. Mertens, H. Struyf, and X. Xu, Dynamics of the drying defects left by residual ultrapure water droplets on silicon substrate, *ECS J. Solid State Sci. Technol.* **1**, P34 (2012).
  - [6] J. Jing, J. Reed, J. Huang, X. Hu, V. Clarke, J. Edington, D. Housman, T. S. Anantharaman, E. J. Huff, B. Mishra, B. Porter, A. Shenker, E. Wolfson, C. Hiort, R. Kantor, C. Aston, and D. Schwartz, Automated high resolution optical mapping using arrayed, fluid-fixed DNA molecules, *Proc. Natl. Acad. Sci. USA* **95**, 8046 (1998).
  - [7] D. Brutin, B. Sobac, B. Loquet, and J. Sampaol, Pattern formation in drying drops of blood, *J. Fluid Mech.* **667**, 85 (2011).
  - [8] J. Boneberg, F. Burmeister, C. Schäfle, P. Leiderer, D. Reim, A. Fery, and S. Herminghaus, The formation of nano-dot and nano-ring structures in colloidal monolayer lithography, *Langmuir* **13**, 7080 (1997).
  - [9] J. Park and J. Moon, Control of colloidal particle deposit patterns within picoliter droplets ejected by ink-jet printing, *Langmuir* **22**, 3506 (2006).
  - [10] F. Carle, S. Semenov, M. Medale, and D. Brutin, Contribution of convective transport to evaporation of sessile droplets: Empirical model, *Int. J. Therm. Sci.* **101**, 35 (2016).
  - [11] K. H. Kang, H. C. Lim, H. W. Lee, and S. J. Lee, Evaporation-induced saline Rayleigh convection inside a colloidal droplet, *Phys. Fluids* **25**, 042001 (2013).
  - [12] H. Hu and R. Larson, Marangoni effect reverses coffee-ring depositions, *J. Phys. Chem. B* **110**, 7090 (2006).

- [13] C. Diddens, Y. Li, and D. Lohse, Competing Marangoni and Rayleigh convection in evaporating binary droplets, *J. Fluid Mech.* **914**, A23 (2021).
- [14] M. Gonuguntla and A. Sharma, Polymer patterns in evaporating droplets on dissolving substrates, *Langmuir* **20**, 3456 (2004).
- [15] G. Li, H.-J. Butt, and K. Graf, Microstructures by solvent drop evaporation on polymer surfaces: Dependence on molar mass, *Langmuir* **22**, 11395 (2006).
- [16] I. A. Grimaldi, A. D. G. D. Mauro, G. Nenna, F. Loffredo, C. Minarini, and F. Villani, Microstructuring of polymer films by inkjet etching, *J. Appl. Polym. Sci.* **122**, 3637 (2011).
- [17] A. Tay, D. Bendejacq, C. Monteux, and F. Lequeux, How does water wet a hydrosoluble substrate? *Soft Matter* **7**, 6953 (2011).
- [18] J. Dupas, E. Verneuil, M. Ramaioli, L. Forny, L. Talini, and F. Lequeux, Dynamic wetting on a thin film of soluble polymer: Effects of nonlinearities in the sorption isotherm, *Langmuir* **29**, 12572 (2013).
- [19] A. Mailleur, C. Pirat, O. Pierre-Louis, and J. Colombani, Hollow Rims from Water Drop Evaporation on Salt Substrates, *Phys. Rev. Lett.* **121**, 214501 (2018).
- [20] G. Bolognesi, C. Cottin-Bizonne, E. M. Guene, J. Teisseire, and C. Pirat, A novel technique for simultaneous velocity and interface profile measurements on microstructured surfaces, *Soft Matter* **9**, 2239 (2013).
- [21] D. Brutin and V. Starov, Recent advances in droplet wetting and evaporation, *Chem. Soc. Rev.* **47**, 558 (2018).
- [22] See Supplemental Material at <http://link.aps.org/supplemental/10.1103/PhysRevFluids.7.093605> for a video of the  $\mu$ -PIV observation of the flows inside the evaporating drop and for simulations at other temperatures and drop radii.
- [23] J. Colombani, Dissolution measurement free from mass transport, *Pure Appl. Chem.* **85**, 61 (2012).
- [24] H. Hu and R. Larson, Analysis of the effects of Marangoni stresses on the microflow in an evaporating sessile droplet, *Langmuir* **21**, 3972 (2005).
- [25] R. D. Deegan, O. Bakajin, T. F. Dupont, G. Huber, S. R. Nagel, and T. A. Witten, Contact line deposits in an evaporating drop, *Phys. Rev. E* **62**, 756 (2000).
- [26] N. Matubayasi, H. Matsuo, K. Yamamoto, S. Yamaguchi, and A. Matuzawa, Thermodynamic quantities of surface formation of aqueous electrolyte solutions: I. Aqueous solutions of NaCl, MgCl<sub>2</sub>, and LaCl<sub>3</sub>, *J. Colloid Interface Sci.* **209**, 398 (1999).
- [27] D. R. Lide, ed., *CRC Handbook of Chemistry and Physics* (CRC Press, Boca Raton, FL, 2005).
- [28] C. Wohlfarth, *Surface Tension of Pure Liquids and Binary Liquid Mixtures* (Springer, Berlin, 2017).
- [29] I. Zaytsev and G. Aseyev, *Properties of Aqueous Solutions of Electrolytes* (CRC Press, Boca Raton, FL, 1992).
- [30] A. I. Volkov and I. M. Zharsky, *Big Chemical Reference Book* (Modern School, Minsk, 2005), in Russian.
- [31] A. Marin, S. Karpitschka, D. Noguera-Marín, M. A. Cabrerizo-Vílchez, M. Rossi, C. J. Kähler, and M. A. Rodríguez Valverde, Solutal Marangoni flow as the cause of ring stains from drying salty colloidal drops, *Phys. Rev. Fluids* **4**, 041601(R) (2019).
- [32] X. Xu and J. Luo, Marangoni flow in an evaporating water droplet, *Appl. Phys. Lett.* **91**, 124102 (2007).
- [33] S. Chatterjee, M. Kumar, J. S. Murallidharan, and R. Bhardwaj, Evaporation of initially heated sessile droplets and the resultant dried colloidal deposits on substrates held at ambient temperature, *Langmuir* **36**, 8407 (2020).